

Chapter 3

Interactions of Hydrogen with Lattice Defects



Materials include various types of lattice defects, either formed during fabrication or introduced during service. The potential energy of hydrogen atoms close to lattice defects is mostly lower than that in regular interstitial lattice sites due to elastic and electronic interactions, as schematically shown in Fig. 1.1. The interactions result in variation of the local hydrogen concentration around defects and alter the densities and structures of defects. Hydrogen embrittlement is a premature fracture derived from the activation of lattice defects. The behavior of lattice defects in the presence of hydrogen is crucial, but observed hydrogen effects are synergistic of contributions of various defects. Understanding the elementary interactions is necessary, but assigning an observed phenomenon to a specific defect type must be careful because of the often cooperative evolutions of defects.

3.1 Dislocations

3.1.1 *Experimental Facts*

Hydrogen embrittlement is a phenomenon that takes place under applied stress and is more or less associated with plastic deformation. Dislocations are the primary player in plastic deformation, and hydrogen effects on mechanical properties have been ascribed mainly to hydrogen interactions with dislocations. However, the structures of dislocations associated with their movements are complicated, like kinks, jogs, tangles, and networks. Further, dislocation movements accompany the creation of point defects, like vacancies and interstitial atoms. The origin of hydrogen effects in plastic deformation is not simple, and the reliability of an experimental deduction of hydrogen interactions with dislocations must be careful on experimental conditions and presumptions in analysis.

3.1.1.1 Internal Friction

Internal friction (IF) is a specific response of dislocations to mechanical stimulations [1]. The IF represents the dissipation of mechanical energy of vibration within the elastic range imposed on the specimen. It is usually expressed in terms of the reciprocal loss factor Q^{-1} defined as $\Delta W/2\pi W$, where W and ΔW are the maximum elastic stored energy and the energy dissipation during one cycle, respectively. The Q^{-1} spectrum against temperature ramp for deformed iron exhibits two peaks, α - and γ -peaks, due to the movement of dislocations [1]. Various mechanisms of IF associated with the movement of dislocations have been proposed [2], and the α - and γ -peaks are ascribed to the double-kink formation of non-screw and screw dislocations, respectively [3].

When hydrogen is present in deformed iron, a peak newly appears at the intermediate between α - and γ -peaks, and it is named the hydrogen cold-work peak (HCWP). An excellent correlation between the peak height and hydrogen concentration was found [4]. The origin of HCWP is hydrogen interactions with dislocations, but the details are not straightforward. Hirth summarized three basic models of HCWP [5]. A simple model of dislocation motion is the string model of a damped oscillation between pinned points on a dislocation line. A model that Schoeck proposed is that dislocation drags the hydrogen atmosphere as it bows out under oscillating stress [6]. Dislocation motion with hydrogen dragging is a thermally activated process accompanying the diffusion of neighboring hydrogen.

The relaxation time τ of IF, i.e., the characteristic time to reach equilibrium, is temperature dependent since it is proportional to the concentration of hydrogen accumulated in dislocations and inversely proportional to the diffusion coefficient of hydrogen near the dislocation core. Then, τ is expressed in terms of the activation energy E_a , which is the sum of the binding energy of hydrogen with dislocation E_b and the migration energy of hydrogen E_m . The magnitude of τ is experimentally obtained from the peak temperature versus oscillation frequency relationship, i.e.,

$$2\pi f \cdot \tau = 1, \quad (3.1)$$

$$\tau = \tau_0 \exp\left(\frac{E_a}{RT}\right), \quad (3.2)$$

$$E_a = E_b + E_m \quad (3.3)$$

The estimation of E_b from observed E_a is somewhat ambiguous since hydrogen mobility close to the core may differ from that in bulk. For the case of high hydrogen concentrations close to saturation, E_a is equal to E_m . Alternatively, the kink-pair formation accompanying drag of hydrogen has been proposed for HCWP [7, 8]. The model is similar to that for α - and γ -peaks and Eq. (3.3) is replaced by

$$E_a = 2E_k + E'_m, \quad (3.4)$$

where E_k is the kink formation energy and E'_m is the activation energy of diffusion along the core. In the literature, most estimations of E_b were made from experiments conducted following Schoeck’s model, and reported values of E_b are around 25 kJ/mol in iron and steels [9–11], as tabulated in Table 3.1. The viability of an employed model depends on experimental conditions such as microstructures, applied stress, temperature, and hydrogen concentration.

A review article on the application of IF to hydrogen embrittlement of steel is in Ref. [12].

Table 3.1 Experimentally estimated interaction energies of hydrogen with traps in cold-worked iron and steels

Material	Strain (%)	E_a (kJ/mol)	E_b (kJ/mol)	E_m (kJ/mol)	Measuring method	Note	References
Very high purity iron	10	32.6			IF		[9]
0.018% C steel	15	29.6			IF		[9]
Pure iron	16	30	17–25	8.4–12.5	IF		[4]
High purity iron	25	35.1	27	8.4	IF		[10]
Mild steel	20	33	26	7	IF		[11]
Type 430 steel	20	75	43	32	IF		[11]
0.16%C steel	30		25		H-absorption		[13]
0.16%C steel	60		36		H-absorption		[13]
Ferritic steels			20		H-permeation		[13]
AISI 4340			30.5		H-permeation	High occupancy	[13]
0.23% C steel			25		H-desorption	High occupancy	[13]
Pure iron	0–80		59.9		H-permeation	High occupancy	[14]

E_a detrapping activation energy, E_b binding energy, E_m migration energy, *IF* internal friction, *High occupancy* under high hydrogen concentrations

3.1.1.2 Hydrogen Permeation

The density of a type of trap and the hydrogen occupation therein are included in the effective diffusion coefficient D_{eff} , Eqs. (2.24) and (2.25), obtained from permeation experiments. In the domain of low coverage, D_{eff} is expressed as Eq. (2.27) [13], and the temperature dependence of D_{eff} and D_L gives the apparent activation energy of permeation as included in the right-hand side of the equation,

$$\frac{\partial \ln D_{\text{eff}}}{\partial(1/T)} = -\frac{E_m}{R} + \frac{K N_x / N_L}{1 + K N_x / N_L} \frac{E_b}{R} \quad (3.5)$$

Oriani [13] analyzed data in the literature on hydrogen permeation or evolution for various steels with and without cold-working [13]. The estimated binding energies, E_b , were in the range of 25–35 kJ/mol, and the density of trapping sites, N_x , was of the order of 10^{25} m^{-3} in steel without cold-work. Both E_b and N_x increased with an increasing amount of cold-work. Assigning the values of N_x and E_b to dislocations assumes that the effects of cold working on D_{eff} are due to the generation of dislocations. However, Oriani suggested that microcrack surfaces are more critical than dislocations for hydrogen trapping in cold-worked steel.

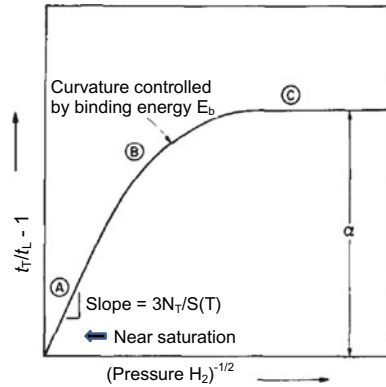
On the other hand, Kumnick and Johnson conducted hydrogen gas permeation-transient measurements for pure iron specimens given cold-working up to 60% [14]. Kumnick and Johnson analyzed the measured time lag data of the permeation using the McNabb–Foster equation for the diffusion accompanying the trapping process. Details of permeation experiments are described in Sect. 4.1. The time lag defined as the intersection of the integrated flux and the time axis varies according to the concentration of lattice hydrogen C_0 , which is a function of the external hydrogen pressure following Sieverts' law given by Eq. 1.1 in Sect. 1.1. The McNabb–Foster equation expresses the time lag using trap parameters p and k in Eq. (2.12). The time lag in the presence of trapping, t_T , is proportional to the purely lattice time lag, t_L , and the ratio t_T/t_L varies according to hydrogen pressure, as schematically shown in Fig. 3.1 [14]. For the dilute occupancy region C in Fig. 3.1 for traps under low hydrogen pressures, t_T/t_L is independent of lattice hydrogen concentration, approximately expressed as,

$$\frac{t_T}{t_L} = 1 + N_T \frac{k}{p} = 1 + \frac{N_T}{N_L} \exp\left(\frac{E_b}{RT}\right), \quad (3.6)$$

where N_T and N_L are densities of the trap and lattice hydrogen sites, respectively. On the other hand, for near saturation region A of traps under high hydrogen pressures, an expression of the ratio t_T/t_L is,

$$\frac{t_T}{t_L} = 1 + \frac{3N_T}{C_0}. \quad (3.7)$$

Fig. 3.1 Schematic diagram of variation of time lag with input hydrogen gas pressure for specimen with saturable traps. t_T and t_L are time lag with and without trapping. $S(T)$ is Sieverts' law coefficient (Kumnick et al. [14])



Trap parameters were determined to fit calculated t_T/t_L with observed values. E_b thus determined was as high as 59.9 kJ/mol for iron given cold-work to 60% at 318 K, far exceeding the values estimated by Oriani. The inferred trap densities were slightly less than 10^{21} m^{-3} for annealed iron and more than 10^{23} m^{-3} for heavily deformed iron. Experiments were conducted under hydrogen gas pressures lower than 0.1 MPa. The pressure was pretty low, but observed time lags decreased with increasing hydrogen pressure suggesting that experiments were in a range for saturated traps.

The entity of the trap corresponding to an exceptionally high E_b of 59.9 kJ/mol was not definite. Kumnick and Johnson suggested some heterogeneous sites along the dislocation core, like jogs or point defect debris left behind by moving dislocations. Kumnick and Johnson also noticed that sensitivities of experimental techniques to defects might differ by the range of trapping parameters.

Table 3.1 includes values of E_b and N_T obtained by IF and permeation experiments. The materials were cold-worked iron and steels, assuming a single type of trap. The binding energies obtained in a substantial experimental range were challenging to ascribe simply to dislocations. The presence of multiple kinds of traps makes transient permeation behaviors dependent on hydrogen concentration, and the kinetics of filling traps differ by E_b of each trap as described in Sect. 2.1.3. Data obtained by IF techniques in Table 3.1 may be reasonably reliable as interaction energies of hydrogen with dislocations in iron, but the precise origins of data obtained by different methods are not yet established.

3.1.1.3 Thermal Desorption Analysis

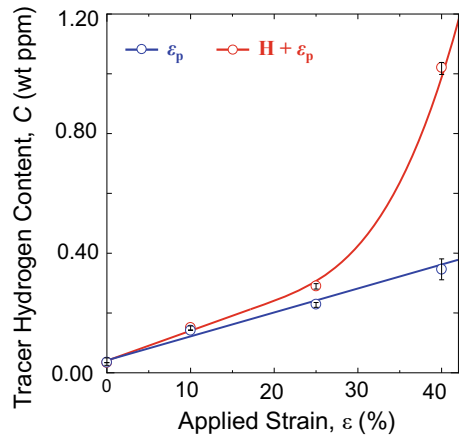
The hydrogen absorption capacity in steel generally increases by plastic straining, indicating an increase in the density of lattice defects that trap hydrogen. Choo and Lee conducted TDA of hydrogen, described in Sect. 2.2.1, introduced to cold-drawn iron bar specimens of 8 mm diameter [15]. Hydrogen was introduced under 0.2 MPa hydrogen pressure at 673 K, and TDA measurements were conducted after degassing

mobile hydrogen at room temperature for six hours, intending to remain only trapped hydrogen. Applying Eq. 2.19 to observed data, E_b was 19.2 kJ/mol by subtracting E_m of 7.6 kJ/mol from E_a of 26.8 kJ/mol. Choo and Lee assumed that remained hydrogen was trapped in dislocations and that desorption was dissociation-controlled. On the other hand, Ono and Meshii conducted TDA of hydrogen electrochemically introduced to a cold-rolled single crystal of pure iron. Assuming diffusion-controlled desorption under dynamic equilibrium between trapping and de-trapping processes described in Sect. 2.2.1.3, E_b of 47 kJ/mol gave good agreement between simulated and experimental TDA profiles [16].

An application of the improved technique of TDA, i.e., LTDS described in Sect. 2.2.1.5 (a), to pure iron is shown in Fig. 2.5. LTDS measured hydrogen introduced as a tracer of lattice defects into tensile-strained specimens with/without hydrogen precharging [17]. Precharged hydrogen was degassed at room temperature after straining. Figure 3.2 shows the increase in the amount of tracer hydrogen with the applied strain, corresponding to the density of trap sites [17]. Cathodic electrolysis for charging tracer hydrogen was mild in a 0.1 N NaOH + 20 g · L⁻¹ of NH₄SCN aqueous solution at 50 A · m⁻². The precharged hydrogen enhanced the strain-induced generation of trap sites, and a crucial fact is that the hydrogen enhancement is not significant in the early stage of straining, but it becomes prominent in a high strain range over 25%. Further findings and consideration are in Sect. 3.2.3.2, concerning a joint function of hydrogen and strain-induced vacancies.

The LTDS profile in Fig. 2.5 exhibits two desorption peaks, and the lower temperature peak is dominant in Fig. 3.2. Sugiyama and Takai separated the two peaks by Gaussian fitting and applied the Choo-Lee method [15] to estimate the activation energy of hydrogen desorption E_a . The obtained values for the lower temperature peak were 30.4 and 38.0 kJ/mol at a plastic strain of 25% and 40%, respectively. On the other hand, E_a for the higher temperature peak were 54.9 and 56.4 kJ/mol. Subtracting E_m of 8 kJ/mol, the hydrogen binding energy E_b of the prominent lower

Fig. 3.2 Tracer hydrogen content as a function of plastic strain applied to iron specimens with (H + ε_p) without (ε_p) hydrogen precharging (Sugiyama et al. [17])



temperature peak is 22.4 and 30.0 kJ/mol at a plastic strain of 25% and 40%, respectively. Sugiyama and Takai assigned the lower temperature peak to mainly desorption from dislocations.

A range of binding energy, not a single value, is suggested in Sect. 2.1.2 for the trap sites composing the lower temperature peak. Complicated structures of dislocation might cause scatter in reported values of E_a and E_b in the literature. Theoretical analyses envisage more details of hydrogen–dislocation interactions.

3.1.2 Theoretical Estimation of Hydrogen–Dislocation Interactions

Interactions of dislocations with interstitial atoms such as carbon and nitrogen have been well studied concerning the yield point phenomena in steel. The primary external factor that affects the potential energy of a hydrogen atom is hydrostatic stress, interacting with the local lattice expansion around the atom. The stress fields around edge dislocations are the first to be examined in this respect.

The interaction energy of a hydrogen atom with the elastic field of an edge dislocation is expressed as [18]

$$W = \frac{Gb(1 + \nu)\delta v \sin \theta}{3\pi(1 - \nu)r}, \quad (3.8)$$

where G is shear modulus, b is Burger's vector, ν is Poisson's ratio, δv is internal volume change around a hydrogen atom, r and θ are cylindrical coordinates fixed on the dislocation line. The volume change δv is 1.2 ml/mol in iron and is related to the partial molar volume V_H by

$$\delta v = \frac{V_H(1 + \nu)}{3(1 - \nu)}. \quad (3.9)$$

The calculated W is 28 kJ/mol for a hydrogen atom located at $r = 0.4$ nm and $\theta = \pi/2$. The elastic field of edge dislocation attracts hydrogen atoms, and Hirth and Carnahan numerically calculated the integral amount of hydrogen atoms for both the Boltzmann and Fermi–Dirac distributions [19]. Results in the two distributions beyond a critical inner cutoff radius of 0.248 nm were similar, but using the Fermi–Dirac distribution was necessary for a near core region.

An atomistic calculation of the distribution and the trap energy of hydrogen around an edge dislocation in iron was conducted by Taketomi et al. [20] The model dislocation was a $\{112\} <111>$ edge dislocation on a $\{112\}$ plane, and the crystalline-disordered region near the dislocation core was of concern. Two types, tetragonal (T) and octahedral (O), of hydrogen occupation sites were considered, and the energy of the system was calculated using an embedded atom method (EAM) potential. Taketomi et al. noticed that both hydrostatic and shear stresses sensitively affect the

hydrogen-trap energy, and strong trap sites distributed on the slip plane around the dislocation core. The calculated hydrogen-trap energy varies by the type of site and the region around the dislocation core. The maximum trap energy in the core was about 42 kJ/mol. Outside of the core, the maximum trap energy was about 12 kJ/mol at a *T*-site below the slip plane, while O-sites showed much higher trap energy in a region along the slip plane.

Straight screw dislocation, on the other hand, has no long-range hydrostatic stress field. Elastic interaction with hydrogen appears in regions near wiggles on a flexible screw dislocation, leading to relatively weak and short-range elastic interactions. The origin of the high potential barrier has been attributed to core structures of screw dislocations [21]. Atomistic simulations have been conducted with different core structures and kink-pair formation [22–25].

Screw components of dislocations are vital in the mobility of dislocations in body-centered cubic metals at low temperatures, and thermal activation of kink pairs mediates the motion of screw dislocation. Wen et al. calculated the energy of a $1/2[111]$ screw dislocation introduced into a supercell in bcc iron using an EAM [26]. One hydrogen atom was placed at various sites in the core, and the binding energy of hydrogen was defined as the difference in energies between the states with and without a hydrogen atom. The binding energies of hydrogen at thirteen sites available to a hydrogen atom in the core were in a wide range between 43 and 4.3 kJ/mol.

On the other hand, Itakura et al. calculated the energy of screw dislocation using the density functional theory, placing a hydrogen atom at each *T*-site near the core [27]. The binding energy E_b of a specific site was defined as the hydrogen solution energy E_s referred to as the bulk *T*-site. The expression of E_s was in the form,

$$E_s = E_{d+H} - E_d - E_{H_2}/2, \quad (3.10)$$

where E_{d+H} , E_d , and E_{H_2} denote dislocation energies with a hydrogen atom, a reference dislocation configuration, and a hydrogen molecule, respectively. Calculated values of E_b varied by the core configuration and the site of a hydrogen atom. The maximum values of E_b in the stable and unstable core configurations were 25 kJ/mol and 38 kJ/mol, respectively. The authors deduced that a hydrogen atom could lower the Peierls barrier by about 12.5 kJ/mol.

Softening or hardening is a crucial issue as the effect of hydrogen on dislocation mobility and the reduction in either kink nucleation enthalpy or kink trapping, respectively, is a suggested mechanism. Atomistic calculations are further described in Sect. 5.5.2 on the mobility of screw dislocations.

Gavriljuk et al. conducted first principles calculations of electronic structures affected by interstitial atoms in fcc iron and applied the results to analyze interactions between dislocations and interstitial atoms [28, 29]. The calculations were for cases of fairly high hydrogen concentrations, 3–5 at% in the atomic ratio [28] or 0.25 or 1.0 in an elementary cell [29]. The results are that hydrogen increases the density of conduction electrons in the vicinity of hydrogen atoms and lowers the shear modulus, the stress for the activation of dislocation sources, the line tension of dislocations,

and the distance between dislocations in the pileups. Similar effects as hydrogen are expected for nitrogen, but the opposite for carbon because carbon decreases the density of conduction electrons around dislocations [28].

Interactions of hydrogen with dislocations strongly depend on the structures of dislocations. Model structures of dislocations employed for theoretical estimations cited above are simplified for the convenience of calculation. Actual densities of dislocations in steel that exhibits hydrogen embrittlement are very high, and inhomogeneous segments on dislocation lines such as kinks, jogs, tangles, and cell configurations induce complex stress and displacement fields.

Alternatively, Kirchheim developed an extensive theory on the stabilization of lattice defects by hydrogen in a thermodynamic scheme [30, 31]. The Gibbs adsorption isotherm claims a change in the surface energy by the adsorption of molecules. By analogy, the total free energy of the system decreases when solute atoms segregate at lattice defects, and the reduction owes to the decrease in the formation energy $d\gamma$ of the defect. The expression of $d\gamma$ in terms of the excess of solute at the defect, Γ , and the change of the chemical potential on segregation, $d\mu$, for a solute A is in the form of

$$d\gamma = -\Gamma_A d\mu_A. \quad (3.11)$$

For dislocation, Γ_A was defined under constant temperature, volume, and chemical potentials of A and the solvent as

$$\Gamma_A = \left. \frac{\partial n_A}{\partial l} \right|_{T, V, \mu_A, \mu}, \quad (3.12)$$

where l is the dislocation length and n_A is the number of A atoms under open system.

The decrease in the formation energy in the presence of hydrogen activates dislocation sources. Then, it was supposed that newly generated dislocations push former dislocations together with the ease of kink pair formation and that the sequence appears as the observed enhanced mobility of dislocations by hydrogen [32]. This defect-acting agent (DEFACTANT) mechanism is general and can be applied to the formation energies of various defects such as dislocations, vacancies, grain boundaries, and crack surfaces [32].

3.2 Vacancies

Vacancies play a crucial role in the creep failure of metallic materials at high temperatures, but their role in hydrogen embrittlement has not been paid much attention. Then, to understand the interactions between hydrogen and vacancies, this section starts with some general attributes of vacancies.

3.2.1 Elementary Attributes

3.2.1.1 Thermal Equilibrium Density

Lattice vacancy is a type of point defect in crystalline materials. It exists inherently with the density C_V for a single vacancy in thermal equilibrium as [33, 34],

$$C_V = A \exp\left(-\frac{H_f}{RT}\right), \quad (3.13)$$

where A is the entropy factor of 1–10 in most metals, and H_f is the formation enthalpy of monovacancy. The magnitude of C_V is directly obtained by subtracting the change of lattice constants from the observed thermal dilatations, and the temperature dependence of C_V gives H_f . Reported values of C_V are minimal, 2.4×10^{-11} , 1.3×10^{-21} , and 7.6×10^{-27} , respectively, for Al, Cu, and α -Fe at room temperatures with $A = 5$. The observed C_V involves clustered vacancies [33]. The values of H_f are 65, 124, and 154 kJ/mol for Al, Cu, and α -Fe, respectively. Such low densities in thermal equilibrium might be a reason why much attention has not been paid to the role of vacancies in mechanical properties.

Positron annihilation spectroscopy (PAS) is another powerful tool for measuring vacancy concentrations [33, 35]. Positrons injected into metal crystals migrate through the lattice before annihilation with electrons, with a lifetime depending on the diffusional path. Vacancies effectively trap positrons because the lifetime of positrons is relatively long near vacancies owing to low electron densities. The enhancement of positron lifetime in vacancies is by 20–80% to that in the perfect lattice. The positron trapping probability in vacancies is proportional to the vacancy concentration. The trapping rate κ_v is expressed as

$$\kappa_v = \mu_v C_V, \quad (3.14)$$

where μ_v is the specific trapping rate for monovacancy and is estimated to be $(1.1 \pm 0.2) \times 10^{15}/\text{s}$ [36]. The value of κ_v is determined from the observed positron lifetime.

Positron annihilation is detected by measuring γ -ray emitted at the time of annihilation. Doppler broadening of annihilation γ -rays is utilized to distinguish annihilations with core and conduction electrons. A trapping model calculates the formation enthalpy H_f from observed Doppler broadening. The obtained values of H_f for pure iron are 173 and 193 kJ/mol in the paramagnetic and ferromagnetic states, respectively [37]. Applications of PAS to hydrogen effects on lattice defects are presented in the following Sects. 3.2.2 and 3.2.3.2(b).

3.2.1.2 Vacancy Generation Associated with Plastic Deformation

The density of vacancies substantially increases associated with plastic deformation. The density of point defects amounting to 4×10^{-5} was estimated from electrical resistivity measurements on annealing iron strained to 20% [38]. The concerning point defects are ascribed mostly to vacancies because the formation energy of vacancy is lower than that of interstitial.

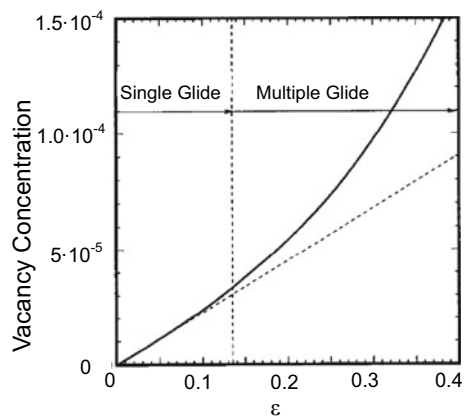
(a) Theoretical Models

Elementary mechanisms of vacancy generation by mutual interactions of moving dislocations are found in textbooks of dislocation theories. Van Bueren considered randomly distributed dislocations that form a spatial network [39]. Each element of the network acts as a dislocation source, and a generated dislocation loop crosses dislocations and forms jogs. The density of point defects left behind in the wake of moving jogs on the dislocation was estimated as $1.3 \times 10^{21} \text{ } \varepsilon^2/\text{cm}^3$ in the case of multiple glides in copper.

Cuttiño and Ortiz considered the motion of jogged screw segments formed by dislocation intersection and by double cross-slip [40]. Computed vacancy concentrations in a uniaxial tension test on copper single crystal oriented for single slip are shown in Fig. 3.3 [40]. Quadratic dependence on strain appears in the multiple glide region, and the expected C_v was as high as 10^{-4} at a strain of 30%. An alternative mechanism of generating a high density of vacancies is mutual annihilation of dislocations of opposite signs, or dislocation dipole, approaching closely neighboring glide planes [41]. The density of point defects depends on the density of dislocations, and a high concentration amounting to 10^{-3} is expected for vacancies in the dislocation-rich walls of persistent slip bands in fatigued copper [41].

Extending the model, Ohashi theoretically examined the pair annihilation of edge dislocations for a copper single crystal [42]. The density of accumulated vacancy varied significantly by the used model. The vacancy density increases with applied strain, and the double-slip condition prominently enhances the increase compared to

Fig. 3.3 Vacancy generation by the motion of jogged dislocations versus axial strain (Cuttiño et al. [40])



the single-slip condition. The vacancy density under the double-slip condition was at the order of $10^{24}\text{--}10^{25}\text{ m}^{-3}$, or $10^{-5}\text{--}10^{-4}$ in atomic ratio, after deforming to a plastic shear strain of 1.

(b) Experimental evidences

An increase in the hydrogen absorption capacity associated with plastic straining is shown in Fig. 3.2. Dislocations would be an intuitive understanding of the increasing trap sites of hydrogen. Figure 3.4a shows the amounts of tritium introduced by cathodic electrolysis into low-carbon ferritic steel tensile-strained to 25% at 298 K and 223 K [43]. The amount of tritium was measured using TDA that showed a single desorption peak in the temperature range between 393 and 423 K. The cathodic electrolysis for Fig. 3.4 was in 1 N NaOH tritiated aqueous solution at a current density of 25 A/m^2 for 2 h. The condition was pretty mild to avoid the formation of extraneous damage in the specimen, and the amount of tritium was expressed in a unit of radioactivity.

Tritium operates as the tracer of lattice defects, and the amount of desorbed tritium is a measure of the density of strain-induced defects. A noteworthy finding in Fig. 3.4(b) was that the increase in the hydrogen absorption capacity almost totally disappeared by aging the strained specimens at temperatures as low as 473 K (200 °C). The density of dislocations must increase with strain, but Fig. 3.4(b) implies that lattice defects concerned with the increase in absorbed tritium are point defects, mostly vacancies, rather than dislocations. The deformation temperature dependence shown in Figs. 3.3 and 3.4(a) is consistent with the primary role of vacancies, considering the favored stability of vacancies at low temperatures. It is also to be noticed

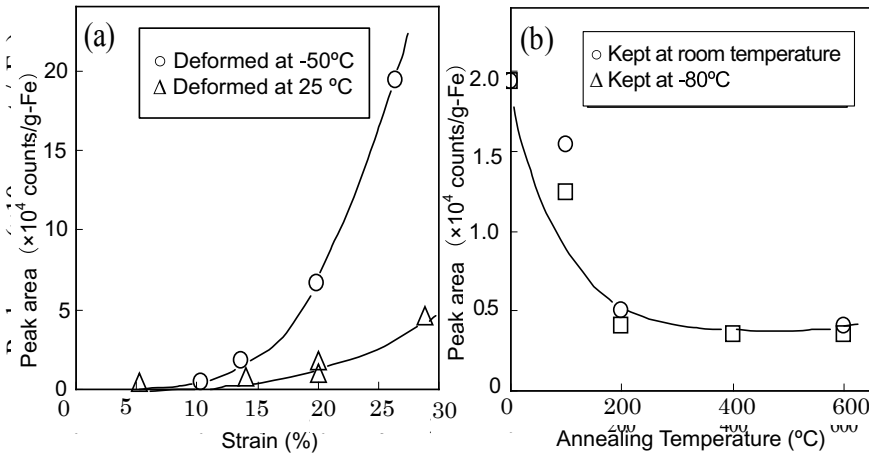


Fig. 3.4 Amounts of tritium absorbed in strained low-carbon ferritic steel. **(a)** Dependence on the amount of strain, **(b)** annealed after straining. The keeping temperature after straining was room temperature or 193 K (Nagumo et al. [16])

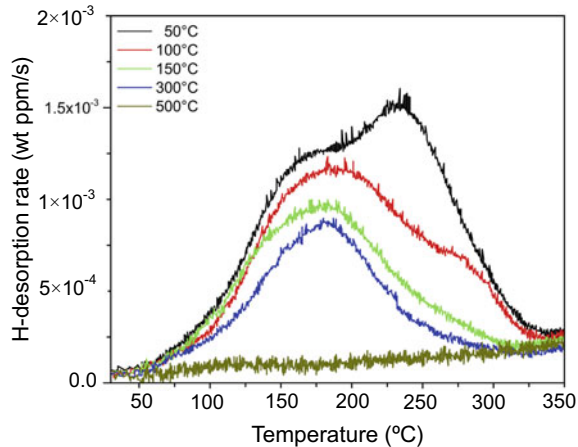
that a substantial increase appears in strain over 10%, consistent with the vacancy generation by mutual interactions of dislocations.

The use of tritium was for convenience, but the reason that Fig. 3.4 detected vacancies rather than dislocations were likely due to the higher hydrogen binding energy of vacancies than of dislocations, together with a low hydrogen fugacity in the experiment. As described in Sect. 2.1.2, the Fermi–Dirac distribution results in preferential hydrogen occupancy in traps of higher binding energies.

Krieger et al. also detected different strain-induced lattice defects using TDA for a 5%Ni–Fe alloy [44]. The alloy was cold rolled to a thickness of 85% reduction and subsequently annealed up to 773 K. Lattice defects in materials were detected using TDA of hydrogen introduced into materials. Hydrogen charging was by cathodic electrolysis in a 0.1 M NaOH aqueous solution at a potential of 1 V (SHE) for 2 h. Figure 3.5 shows TDA profiles at different stages of annealing, keeping for 2 h at each stage [44]. The initial profile exhibited unseparated two peaks. Changes in the profiles on elevating annealing temperature first appeared at the 373 K (100 °C) annealing as the decrease in the desorption peak at around 503 K (230 °C). Subsequently, a substantial decrease appeared at around 523 K (250 °C) by the 423 K (150 °C) annealing. The TDA profile showed a single peak by annealing at above 423 K (150 °C), and the peak disappeared by the 773 K (500 °C) annealing.

The trap sites for the desorption peak finally disappeared by the 773 K annealing and are reasonably ascribed to dislocations. Desorption to be ascribed to dislocations is not present in Fig. 3.4. A likely reason is a much higher dislocation density in Fig. 3.5 compared to Fig. 3.4 because of a higher amount of given plastic strain, 85% versus 25%, in Fig. 3.5. Another conceivable reason is a difference in hydrogen fugacity that, as described in Sect. 2.1.2, controls the partition of hydrogen among trap sites of different hydrogen binding energies. However, a quantitative comparison is not at hand.

Fig. 3.5 TDA profiles of hydrogen introduced to 5%Ni–Fe alloy cold-strained and annealed at various temperatures (Krieger et al. [44])



On the other hand, the desorption composing higher peak temperatures is ascribed to vacancies, consistent with Fig. 3.4. The two-stage decreases in elevating annealing temperature imply multiple structures of vacancies. Clustering stabilizes vacancies, and vacancy clusters are a viable type of defects that compose a part of the higher temperature peak in Fig. 3.5.

3.2.2 Vacancy Clustering and Migration

Vacancies form clusters and vacancy–impurity complexes during migration, reducing the energies of vacancies. The formation enthalpy of a vacancy cluster of order n , $H_{f,nv}$, is defined as

$$H_{f,nv} = nH_{f,1v} - H_{b,nv}, \quad (3.15)$$

where $H_{b,nv}$ is the binding enthalpy of an n -cluster. The $H_{b,nv}$ depends on the configuration of the vacancy cluster, and a first-principles calculation of $H_{b,nv}$ was conducted for various configurations in α -iron [45]. The most stable configurations of n -vacancies in bcc structures are compact clusters, followed by decreasing stability order, double layers, linear chains, tetravacancies, single layers, trivacancies, and divacancies. Calculated dissociation energies of vacancy clusters of $V_n \rightarrow V_{n-1} + V_1$ increase with increasing cluster size, i.e., 85, 94, 117, 140 kJ/mol for $n = 2, 3, 4, 6$, respectively, and almost constant for $n > 6$.

Positron annihilation spectroscopy is a valuable tool for detecting vacancy clusters, and positron states thereof have been calculated using the density functional theory [46]. Calculated positron binding energies and lifetimes for vacancy clusters shown in Fig. 3.6 [46] are listed in Table 3.2 [46]. When multiple traps are present, the observed positron lifetime τ is a weighted mean of lifetime components τ_i in each trap, i.e.,

$$\tau = \sum_{i=1}^N I_i \tau_i. \quad (3.16)$$

On isochronal annealing from 77 K for high-dose electron-irradiated pure iron, a two-step decreases at about 220 and 350 K appeared as shown in Fig. 3.7 [36] for the short positron lifetime component τ_1 in a two-components analysis of τ . Alternatively, a long-lifetime component τ_2 appeared at 220 K, extended its value gradually on increasing the annealing temperature, and finally disappeared at about 500 K. The decrease in τ_1 and the appearance of τ_2 components at 220 K were ascribed to the thermally activated mobilization of monovacancies introduced by irradiation and the formation of small clusters. Successive increase in τ_2 was likely due to the increasing cluster size as shown in Table 3.2. The disappearance of τ_2

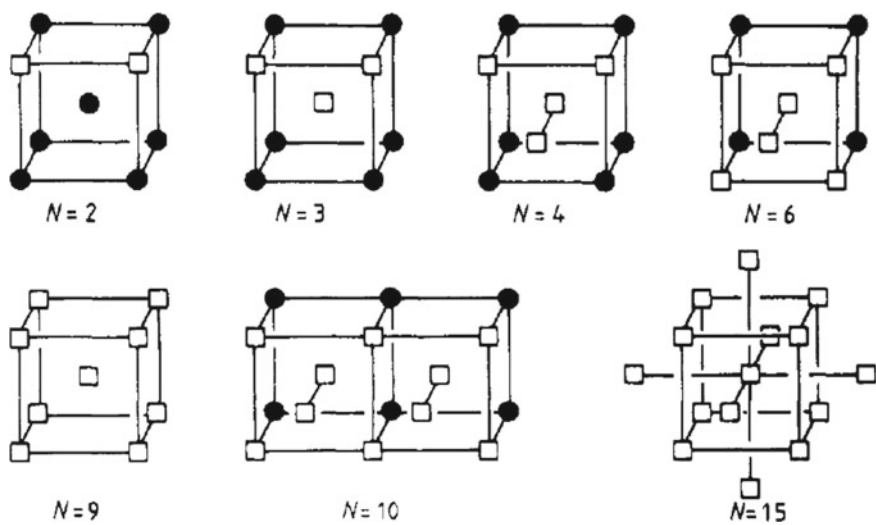


Fig. 3.6 Vacancy agglomerates in bcc structures. N is the number of vacancies (open square) in the agglomerate. Filled circles denote lattice sites (Puska et al. [46]. Reprinted with permission from IOP Publishing)

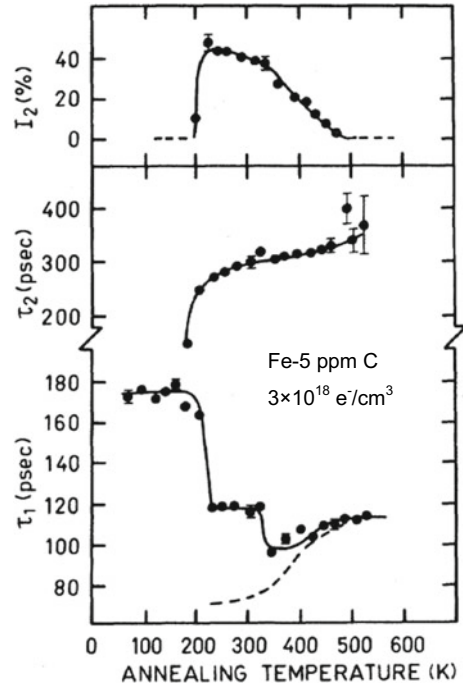
Table 3.2		Calculated positron lifetime τ and binding energy E_b in vacancy clusters in Fe and Ni					
Number of vacancies		1	2	3	4	6	10(Fe) 13(Ni)
Fe	τ (ps)	190	197	232	262	304	334
	E_b (eV)	3.0	4.0	5.6	6.6	7.7	8.6
Ni	τ (ps)	184	203		263	288	376
	E_b (eV)	2.6	3.8		5.9	6.8	9.2

Puska et al. [46]. Reprinted with permission from IOP Publishing

component at 500 K was ascribed to full annealing out of vacancy clusters and annihilation of dissociated vacancies [36].

Interstitial impurities trap migrating vacancies, and free carbon atoms form carbon–vacancy pairs or complexes [36]. For iron carbon-doped by 50 and 750 ppm, the decrease in τ_1 at 220 K indicated that the tendency to form vacancy clusters decreased with the carbon addition. For iron further carbon-doped by 750 ppm, the short positron lifetime τ_1 after the drop at 220 K was still higher than that in pure iron [36]. The phenomenon was ascribed to the capture of migrating vacancies by carbon atoms, forming immobile carbon–vacancy pairs at the expense of forming vacancy clusters. The positron lifetime of the carbon–vacancy pair was estimated to be about 130 ps, much less than 190 ps for monovacancy. It was also suggested that the onset of free migration of carbon at 350 K caused further decoration of carbon–vacancy pairs, no longer having positron trapping capability. The capability of positron-capture of carbon–vacancy complexes is likely less than vacancy clusters,

Fig. 3.7 Positron lifetime parameters versus isochronal annealing temperature in the high-dose electron-irradiated pure iron (Vehanen et al. [36]. Reprinted with permission from American Physical Society)



but it remains on isochronal annealing above 350 K and disappears at 500 K due to the dissociation of the complexes [36].

Vacancies are mobile even at temperatures as low as 220 K in α -iron, but large three-dimensional clusters are immobile. The smallest immobile cluster is the tetravacancy. From the growth rate of interstitial-type dislocation loops introduced by electron irradiation, the estimated activation energy of migration of a single vacancy in iron was 120 kJ/mol [47]. On the other hand, calculated migration energies of mono-, di-, and tri-vacancies in α -iron are in the range of 63.7–65.6 kJ/mol [41]. It is to be noticed that vacancy clusters must dissociate to migrate. In fcc metals such as Au, Al, and Pt, calculated migration energies are in the decreasing order from mono- to trivacancies [48]. A possible reason is that relatively loosely bound trivacancy is more mobile than divacancy, which in turn is more mobile than monovacancy [48]. The disappearance of positron capture at 500 K implies that the dissociation of vacancy clusters takes place and that migrating vacancies annihilate in sites such as dislocations, grain boundaries, and surfaces.

An electrical resistivity measurement is also used to detect lattice defects. The resistivity of pure iron increases by cold work, and the strain-induced resistivity recovers on isochronal annealing. The recovery from room temperature to 673 K was somewhat gradual, and then two stages appeared, the one centered around 753 K and the other distinctly at 823 K [38]. The recovery that continued to 713 K was ascribed to the annihilation of point defects that amounted to the density of 10^{-5} . The further

recovery was ascribed to the reduction in the density of dislocations that amounted to 10^{10} cm^{-2} . Annealing out of vacancy clusters at about 600 K and dislocations at above 800 K was also detected using PAS for pure iron plastically deformed by 60% [36].

The temperature at which recovery occurs on isochronal annealing varies not only by the presence of impurities but also by the concentration of vacancies. A decrease in the recovery temperature associated with increased quenching temperatures was observed in Au and Al corresponding to increased concentrations of quenched-in vacancies [48].

3.2.3 Interaction of Hydrogen with Vacancies

3.2.3.1 Binding Energy and Trapping-Configuration

The elementary factor determining the stability of vacancies is its formation energy, Eq. 3.13, and binding with hydrogen lowers the energy of vacancies. Measurements of the binding energy of hydrogen with vacancies in metals were conducted extensively by Myers et al. by means of deuterium implantation methods [49–54]. Deuterium was ion-implanted at 15 keV into pure iron and formed a deuterium-rich zone close to the surface, accompanying irradiation-induced defects [49]. Subsequent temperature ramp caused diffusion of deuterium. The deuterium concentration in the implanted zone was detected using a 0.7 meV ^3He ion beam that yielded counting protons by the $\text{D}(^3\text{He}, \text{p})^4\text{He}$ nuclear reaction on the impingement. The release of deuterium from the implanted zone occurred in two stages on the temperature ramp, and each stage was mathematically modeled using diffusion equations of the McNabb–Foster type, Eqs. (2.11) and (2.12), which included trapping terms. Trapping parameters were determined numerically to fit the theoretical calculation to experimental data. A sharp release stage centered around 260 K was ascribed to the migration of de-trapped deuterium from deuterium–monovacancy pairs of 46 kJ/mol in the binding enthalpy. The successive release stage in 350–450 K was ascribed to de-trapping from a small vacancy cluster with the binding enthalpy of about 78 kJ/mol [49]. The figures were corrected later to 51 and 69 kJ/mol, respectively, in a modified experiment that suppressed the loss of deuterium from the surface [50].

Binding enthalpies of hydrogen with vacancies in various metals obtained by ion-implantation methods are listed in Table 3.3. In austenitic stainless steel, all release data of deuterium are approximately consistent with trapping at a single binding enthalpy of $\sim 22 \text{ kJ/mol}$ [51]. It is also to be noticed that the binding energy with vacancies is altered by multiple trapping of hydrogen as described shortly.

Experimentally obtained binding enthalpies were theoretically rationalized, referring to the location of hydrogen atom neighboring vacancies. A ^3He ion-channeling measurement for deuterium in an iron single crystal, with the binding energy of 46 kJ/mol, revealed that the deuterium atom displaced by 0.04 nm from the octahedral position along a $\langle 100 \rangle$ direction toward a nearest-neighbor vacancy site [49].

Table 3.3 Binding energies of deuterium with vacancies produced by ion implantation

Material	E_{V-H} (kJ/mol)	Type of vacancies	References
Fe	46	Monovacancy	[48]
Fe	51	Monovacancy	[49]
Fe	68	Cluster	[49]
Fcc stainless steel	22	Cluster	[50]
Ni	23	Monovacancy	[51]
Ni	41	Multivacancy	[51]
Cu	41	Monovacancy small cluster	[52]
Mo	111	Cluster	[53]
Mo	99	Monovacancy (Low occupancy)	[53]
Mo	77	Monovacancy (High occupancy)	[53]

The displacement is because a deuterium atom seeks the optimum electron density to minimize its energy. The binding energy of the hydrogen atom calculated using an effective medium theory (EMT) was consistent with the observed one when a displacement of 0.05 nm was assumed [55].

There are 6 *O*-sites and 8 or 24 T-sites in the fcc or bcc structure, respectively, around a vacant lattice site. Multiple occupations by hydrogen were deduced experimentally from ion implantation experiments of deuterium with different fluencies. Figure 3.8 [56] shows the effects of deuterium fluence on the retained concentrations of deuterium in the implanted zone in iron after a linear temperature ramp. The deuterium concentration decreased at 220 K, and the decrease was enhanced by increasing the deuterium fluence. The shift of the start of deuterium migration to lower temperatures was ascribed to the release of deuterium from multitrapped states at monovacancy when the binding energy decreased with the increasing number of trapped deuterium atoms.

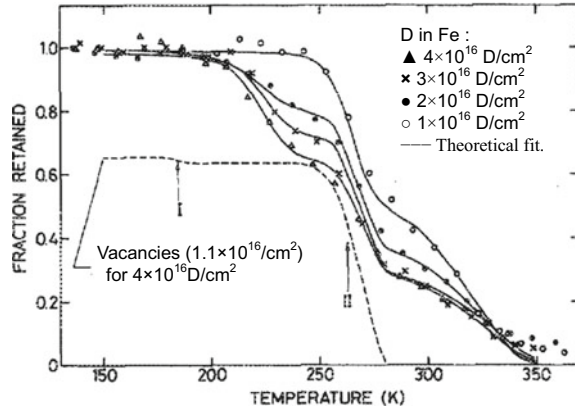
Binding enthalpies were also calculated using EMT for occupancy of 1–6 deuterium atoms for a vacancy in transition metals [57]. In EMT calculations, the binding energy is defined as the energy required to embed a hydrogen atom into the host metal, and the hydrogen trapping energy in multiple occupancies is defined, for the last hydrogen atom in a VH_N complex, as

$$\Delta E(N) = E(N) - E(N - 1) - E_{sol},$$

(3.17)

where E_{sol} denotes the interstitial binding energy [57]. The observed profiles in Fig. 3.8 agree with those calculated using trapping enthalpies of 61 kJ/mol for $N =$

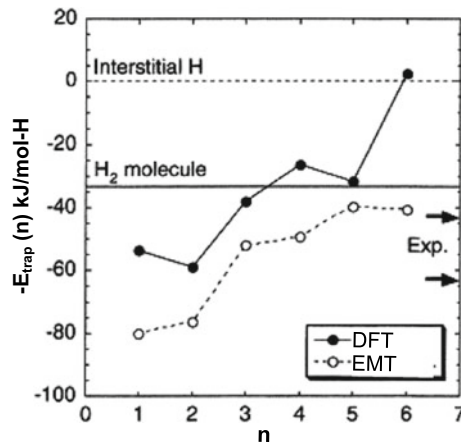
Fig. 3.8 D retention versus temperature profile of 15-keV D in Fe. Strong He traps located at 1.2 μm act as sinks for the released (Besenbacher et al. [56]. Reprinted with permission from AIP Publishing LLC)



1–2 and 41 kJ/mol for $N = 3$ –6 [55]. The results implied decreasing trapping strength with increasing occupancy. Trapping energies calculated afterward using a modified EMT are included in Fig. 3.9 [58] with open circles.

Trapping energies for multiple hydrogen occupancy for a monovacancy were calculated for iron using the density functional theory (DFT) [58, 59]. Calculated trapping energies of VH_N complexes in iron are shown in Fig. 3.9, together with the former results of EMT calculations [56]. The DFT calculation shows that the trapping energies of VH_1 and VH_2 are about 60 kJ/mol and that VH_6 is unstable. The calculation also shows that up to three hydrogen atoms are exothermically bound to monovacancy. Accordingly, very high site occupancies of hydrogen are expected for VH and VH_2 , and most vacancies may exist in the form of VH_2 [59]. Another atomistic calculation using DFT combined with molecular dynamics (MD) and Monte Carlo methods [60] showed that a three-dimensional tetrahedral configuration has the lowest energy for VH_4 and that the binding is exothermic.

Fig. 3.9 Hydrogen trapping energy in α -Fe calculated using DFT (filled circle) and EMT (open circle) (Tateyama et al. [58]. Reprinted with permission from American Physical Society)



An explanation of the stability, deduced by the DFT analysis, was that Fe3d-H1s hybridization causes charge transfer to the region around the hydrogen atom from neighboring iron atoms. Resulted negatively charged hydrogen atoms might repel each other, and calculations showed that distances between hydrogen atoms and the corresponding *O*-sites in the VH_N complexes decrease with increasing *N* [58].

The hydrogen binding energy for multiple trapping in vacancy clusters was calculated by Ebihara et al., using the molecular static simulation [61]. The number of trap sites of an *i*-size vacancy cluster increases with the vacancy cluster size. Table 3.4 lists the calculated hydrogen trapping energies.

3.2.3.2 Hydrogen Enhancement of Strain-Induced Generation of Vacancies

(a) Results of thermal desorption analysis

TDA of hydrogen introduced into deformed iron, used as the tracer of defects, Figs. 3.2 and 3.4, revealed the strain-induced generation of lattice defects. Figure 3.10 [62] is a complementary result of Fig. 3.4, to demonstrate the hydrogen effects on the strain-induced generation of lattice defects. The ordinate of Fig. 3.10 is the amount of tracer hydrogen introduced to saturation into a commercial pure iron given various amounts of tensile-straining after hydrogen precharging. Cathodic hydrogen charging was at a current density of 50 A m² in an aqueous solution of H₂SO₄ of 2.5 in pH added 0.09 mass% NH₄SCN as a catalysis [62]. In Fig. 3.10, the tracer hydrogen is denoted as [strain], [H + strain], and [H + strain + 200 °C], each respectively indicating “strained”, “strained after hydrogen precharging”, and “annealed at 200 °C (473 K) after hydrogen precharging and straining”. The amount of tracer hydrogen was measured using TDA that showed a single desorption peak, and the annealing effect indicates that most of the increment of tracer hydrogen by hydrogen precharging is due to the enhanced generation of vacancies.

LTDS that starts temperature ramp from a temperature as low as 70 K is a powerful tool to exhibit a complete hydrogen thermal desorption profile, as described in Sect. 2.2.1.5(a). In the experiment for Fig. 3.10, a conventional TDA technique could not exhibit a complete desorption profile. Figure 3.11 [63] shows LTDS profiles of tracer-hydrogen introduced into pure iron tensile strained up to 20% with and without hydrogen precharging. Charging of tracer hydrogen was by immersing specimens in an aqueous solution of 20% NH₄SCN at 323 K. The amount of the tracer-hydrogen increases with strain, and hydrogen precharging evolved a new peak at a higher temperature.

The LTDS profiles corresponding to Fig. 3.2 are shown in Fig. 2.5 for the hydrogen-precharged and 25% strained specimen. The existence of a subpeak is evident at the higher temperature side. Figure 3.2 indicates that hydrogen precharging enhances the strain-induced generation, prominently at strain of more than 25%, i.e., when the dislocation density is substantial. In the LTDS profiles shown in Fig. 2.5, the lower temperature peak is ascribed to the desorption from dislocations, as described

Table 3.4 H-Trapping energy for vacancies and vacancy clusters (Ebihara et al. [61])

Trapped H atom	V1	V2	V3	V4	V5	V6	V7	V8	V9
1	53.3	56.9	54.9	55.3	55.4	55.4	55.9	55.9	56.8
2	50.0	53	54.5	55.4	55.4	55.4	55.7	55.9	55.9
3	32.5	52.7	54.3	55.1	55.1	55.4	55.7	55.9	55.9
4	27.5	36.5	50.9	55.1	55.1	55.4	55.4	55.9	55.9
5	17.6	37.8	50.1	50.8	54.8	54.9	55.1	55.4	55.5
6	10.6	38.6	44.9	50.9	51.1	54.9	55.1	55.4	55.4
7		28.1	34.8	50.3	51.2	52.4	54.9	55.2	55.5
8		28.4	34.4	50.4	50.6	52.5	51.5	55.2	55.2
9		19.1	33.4	30.9	50.0	50.1	51.2	51.5	55.1
10		18.2	26.0	31.1	37.0	50.1	47.0	51.6	52.4
11		10.1	24.3	30.5	38.0	37.1	47.4	50.4	51.6
12			7.9	27.6	35.5	37.1	51.1	50.7	51.4
13			13.1	23.9	29.8	40.0	42.5	45.9	51.1
14				18.2	24.5	34.6	36.8	45.7	51.1
15				17.6	26.6	30.0	34.5	36.6	50.2
16				13.8	21.5	29.4	32.9	36.0	37.4
17					20.6	26.4	32.9	35.5	38.8
18					14.8	26.3	30.9	34.1	35.8
19					10.6	16.5	28.3	33.6	33.1
20						14.8	25.5	29.0	33.3
21						12.7	21.3	26.7	30.9
22							17.7	26.4	31.4
23							15.9	24.3	29.4
24							13.1	22.4	25.8
25								16.9	22.6
26								12.6	22.2
27									20.1
28									16.0
29									13.4

in Sect. 3.1.1.3. Figure 3.12 [17] shows the hydrogen enhancement of the two peaks in Fig. 2.5, expressed as the ratio of the peak intensities with and without hydrogen precharging.

Obviously, the hydrogen enhancement appears in the higher temperature peak 2, while the lower temperature peak 1, which originates in trapping in dislocations, appears at a strain of more than 25%. It implies that hydrogen enhancement is more prominent for vacancies than for dislocations in the early stage of plastic deformation.

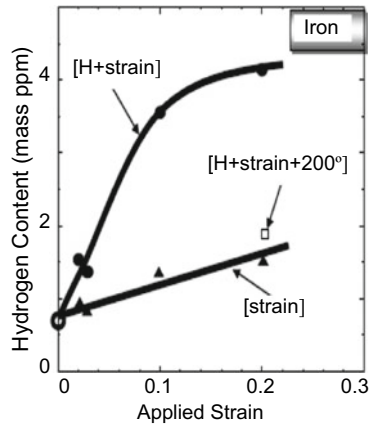


Fig. 3.10 Amounts of the tracer-hydrogen introduced to iron specimens after straining [strain], strained after hydrogen-precharging [H + strain], and further annealing at 473 K (200 °C) [H + strain + 200 °C] (Takai et al. [62])

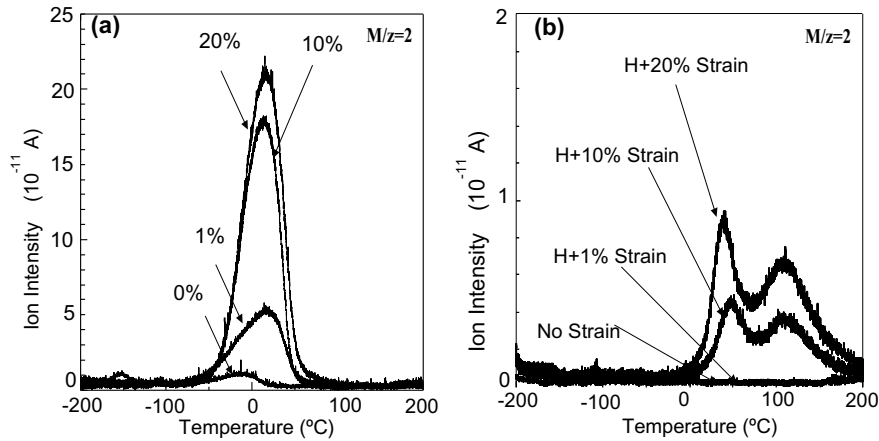
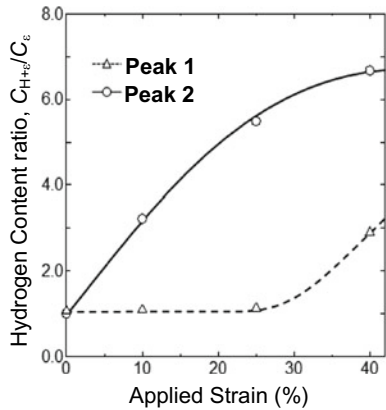


Fig. 3.11 LTDS profiles of hydrogen introduced into iron specimens given strain up to 20% (a) without and (b) with hydrogen precharging. The thickness of specimen and the concentration of NH_4SCN are 0.3 mm and 20% at 323 K (50 °C) for (a) and 0.4 mm and 0.05% at 303 K (30 °C) for (b), respectively (Sato et al. [63]. Reprinted with permission from The Iron and Steel Institute Japan)

Ebihara et al. simulated the LTDS profile shown in Fig. 2.5 for α -iron using a model incorporating vacancies and vacancy clusters [61]. The model considered up to nine-vacancies cluster, V_9 , and employed parameters, including the hydrogen trapping energy of vacancies and vacancy clusters based on atomistic calculations. The solution of the McNabb–Foster equation used the finite difference method. Simulations were initially conducted for the degassing, annealing, polishing, and charging

Fig. 3.12 Ratio of tracer hydrogen contents introduced to strained iron specimens with and without hydrogen precharging. Two peaks in Fig. 2.5 are separated by Gaussian fitting as a function of applied plastic strain (Sugiyama et al. [17])



processes before the LTDS measurements. Annihilation, dissociation, and clustering proceed during the processes. Figure 3.13 compares the densities of vacancy clusters during heating process for strained specimens with and without hydrogen charging [61]. V_4 and V_5 are relatively more stable compared with V_2 and V_3 , and hydrogen favors the stability. However, the results strongly depend on presumptions for the simulation, and a quantitative comparison with experimental results is difficult.

The thermal stability is a measure for identifying the type of lattice defects. Figure 3.4(b) shows that tritium trap-sites are annihilated by annealing at temperatures as low as 473 K (200 °C) as described about Fig. 3.4. Figure 3.14 [17] shows similar aging results for the LTDS peaks of tracer hydrogen shown in Fig. 2.5. The specimens were strained to 25% with/without hydrogen precharging and were subsequently aged at various temperatures up to 423 K for 1 h. Cathodic electrolysis to

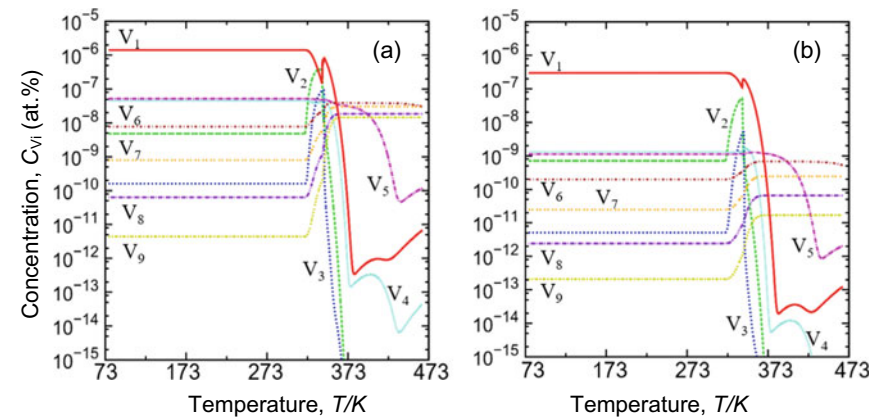
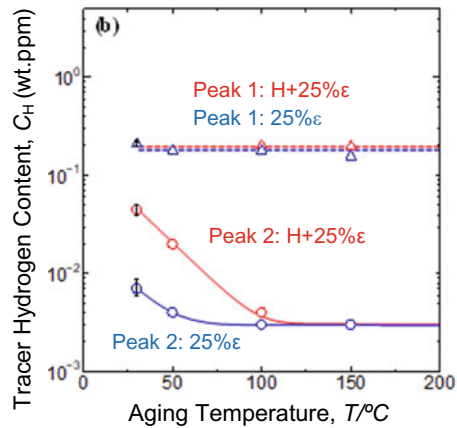


Fig. 3.13 Calculated densities of vacancy clusters during the heating process in LTDS of 25% tensile-strained iron. Straining is at 303 K (a) without and (b) with hydrogen precharging (Ebihara et al. [61])

Fig. 3.14 Tracer hydrogen contents in Peak 1 and 2 of LTDS profile, shown in Fig. 2.5, after aging at various temperatures of 25% strained pure iron with and without hydrogen precharging (Sugiyama et al. [17])



introduce tracer-hydrogen was in a 0.1 N NaOH aqueous solution with $20 \text{ g} \cdot \text{L}^{-1}$ of NH_4SCN . The trap sites composing the higher temperature peak gradually decreased by elevating the aging temperature and almost totally annihilated at 373 K. On the other hand, the lower temperature peak was hardly affected by aging at temperatures up to 423 K.

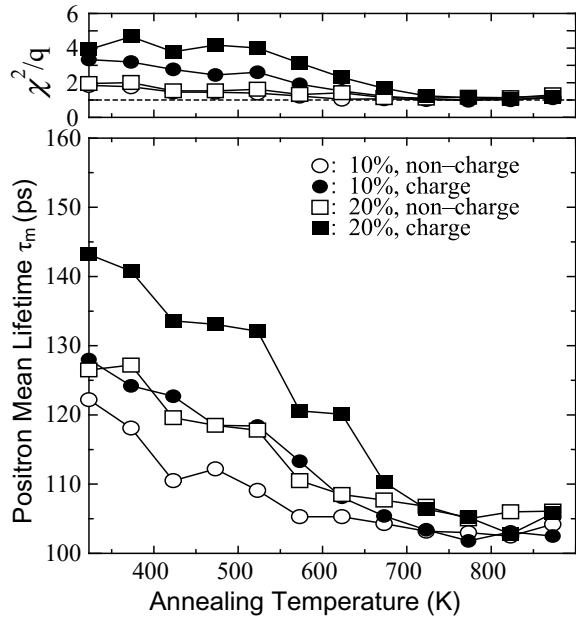
The results are consistent with identifying the trap sites, dislocations, and vacancies to the lower and higher temperature peaks, respectively. *Hydrogen enhancement was preferential for the generation of vacancies rather than dislocations.* TDA in Fig. 3.10 started the temperature ramp from room temperature without showing separation of the peak. A substantial loss of diffusive hydrogen before the start of TDA might have failed to detect the desorption peak from dislocations.

(b) Results of positron annihilation spectroscopy

Positron annihilation spectroscopy (PAS), sensitive to vacancies, is a more direct method than TDA to investigate the nature of lattice defects. Some applications are described in Sects. 3.2.1 and 3.2.2. Figure 3.15 [64] shows the mean positron lifetime τ_m in pure iron on isochronal annealing after tensile straining at room temperature with and without hydrogen precharging. The increase in τ_m by straining is enhanced by the presence of hydrogen at the time of straining. Annealing at 900 K reduced τ_m to $100 \pm 2 \text{ ps}$ which is coincident to the calculated τ in the α -Fe lattice [46]. The variances, χ^2/q , larger than 2.0 for τ_m in deformed iron indicate that τ_m is composed of multicomponents.

Significant recoveries of τ_m that appear at about 400 K, 550 K, and 650 K were analyzed for components. Figure 3.16 [64] shows results for specimens deformed by 20% (a) without and (b) with hydrogen precharging. In the annealing temperature range from 400 to 625 K, the longer lifetime in two-component analyses was 150 ps, coincident with a calculated τ in dislocations [65]. At temperatures lower than 375 K for (a) and 575 K for (b), three-component analyses gave the longest life component

Fig. 3.15 Positron mean lifetime during isochronal annealing of iron deformed with and without hydrogen precharging. Filled marks denote hydrogen-precharged specimens (Sakaki et al. [64])



τ_3 exceeding 400 ps. The recovery stage corresponds to the annihilation of vacancies, and τ_3 indicates positron lifetime likely in large vacancy clusters.

Figures 3.15 and 3.16 exhibit hydrogen effects, i.e., increasing τ_m and retaining the longest lifetime component τ_3 at high temperatures. The relative intensity of the τ_i component is related to the positron-trapping probability κ_i in Eq. (3.14), and κ_i is proportional to the concentration of the i -th defect C_i [36, 65]. The estimated densities of dislocations and vacancies are listed in Table 3.5 [64]. The density of dislocations increases with the amount of plastic strain, as expected, but hydrogen does not affect the increase in the dislocation density. On the other hand, a substantial enhancement by hydrogen is evident for the strain-induced generation of vacancies. These PAS measurements are consistent with the TDA results shown in Figs. 3.10 and 3.12, manifesting the preferential effect of hydrogen on the strain-induced generation of vacancies rather than dislocations.

The hydrogen-enhanced increase in positron lifetime has been observed for various deformed materials; AISI 410 martensitic steel [66], Ni single crystal and Ni-alloy [67], α -iron [68], Type 316L stainless steel [69, 70], Type 304 stainless steel [71], and martensitic steel [72]. The clustering of vacancies is crucial to the nanovoid nucleation in the fracture process. TDA in Fig. 3.5 and PAS in Fig. 3.15 exhibited the presence of clusters of strain-induced vacancies. Sugita et al. analyzed positron lifetime data for martensitic steel and showed that hydrogen promoted the clustering of vacancies [66]. Chiari et al. showed for α -iron that decreasing the strain rate increases the lifetime, and that clustering is prominent at temperatures over 350 K [68].

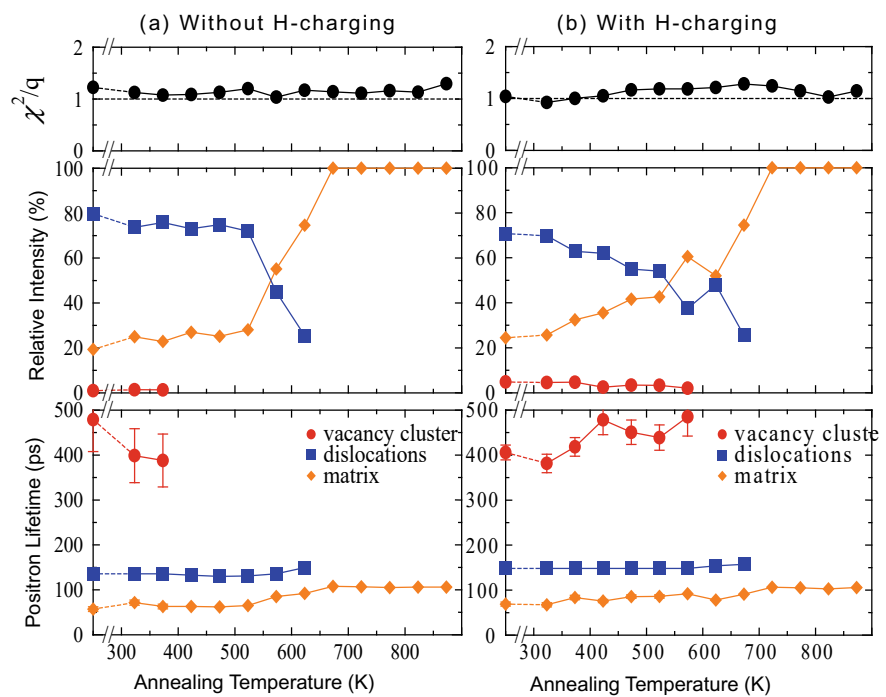


Fig. 3.16 Components of mean positron lifetimes τ_m shown in Fig. 3.15 and their relative intensities (Sakaki et al. [64])

Table 3.5 Densities of dislocations (C_d) and vacancies (C_v) in iron deformed with/without hydrogen precharging

Strain (%)	Hydrogen	C_d ($10^{10}/\text{cm}^2$)	C_v (10^{-7})
10	None	1	Not detected
	Charged	0.9	1.7
20	None	2.2	1.7
	Charged	1.9	8.2

Measurements by positron annihilation spectroscopy (Sakaki et al. [64])

Hydrogen hardly affected the positron capture at dislocations [66], but a grain size dependence of positron lifetime and its relative intensity was observed in Ni-alloys given hydrogen precharging and straining [67]. The evolution of the long-time life component of the lifetime is preferential in small grain size specimens, and the suggested origin was vacancy agglomeration on grain boundaries and in the adjacent volumes [67].

3.2.3.3 Theoretical Background for a High Density of Vacancies

The thermal equilibrium density of vacancies increases with the decrease in the formation enthalpy of vacancies, as Eq. (3.13) states. When the DEFACTANT mechanism by Kirchheim, described in Sect. 3.1.2, is applied to vacancies that combine with hydrogen, the formation enthalpy of vacancies H_f is related to the logarithm of hydrogen activity as expressed in the form

$$\frac{\partial H_f}{\partial \ln a} = -RTZ, \quad (3.18)$$

where Z is the average number of hydrogen atoms per vacancy [31]. A DFT calculation of the total energy of vacancy–hydrogen complex by Tateyama and Ohno [58] showed a substantial decrease in H_f of a VH_N complex, occasionally to negative values, under high hydrogen pressures of 1–2 GPa and Z of 5 or 6. However, the expected densities of vacancies are still very low in *thermal equilibrium* in most situations where hydrogen embrittlement appears.

Another mechanism of realizing high densities of vacancies is kinetic effects. Excess vacancies generated by mutual interactions of dislocations are unstable and tend to annihilate at various sinks such as dislocations, grain boundaries and surfaces. Migration of vacancies is requisite for this annihilation process. However, the formation of immobile clusters and complexes with impurity atoms impede the migration, as described in Sect. 3.2.2, and retard annihilation, keeping high densities before reaching thermal equilibrium.

The mobility of a single vacancy in bcc iron under a hydrogen environment has been calculated using the DFT and the nudged elastic band method to find the diffusion path of the minimum energy [59]. A configuration, i.e., two hydrogen atoms trapped at opposite O -sites across a vacancy, has the highest binding energy, and the fraction of the VH_2 complex is predominant at room temperature. In that configuration, the activation energy of vacancy diffusion increases from 60 to 103 kJ/mol, and the frequency decreases from 1.71×10^{-2} to $1.62 \times 10^{-8} \text{ s}^{-1}$, showing almost immobile vacancies. Consequently, for the generation of vacancies by jog dragging of screw dislocations, high densities of vacancies are expected to remain behind moving screw dislocations [59].

Luna et al. conducted some first principles calculations of positron lifetimes and momentum distributions for vacancy clustering in pure metals [73].

3.3 Precipitates

Fine carbides or nitrides are widely utilized for grain refinement and precipitation hardening of steel. Interactions of hydrogen with such precipitates are crucial for hydrogen embrittlement of high-strength steel, and many studies have been reported. Experiments to obtain binding energies mainly address diffusion or permeation

processes in which hydrogen trapping and de-trapping occur, as described concerning TDA in Sect. 2.2.1.3.

3.3.1 TiC

TiC is the most extensively studied precipitate. Asaoka et al. visualized the distribution of tritium introduced into a Fe-0.15%Ti alloy using tritium autoradiography and examined the thermal desorption and associated changes of the distribution of tritium [74]. A release of tritium from an incoherent TiC/matrix interface occurred at 873 K, and the trapping enthalpy calculated using Oriani's diffusion equation [13] was 71–79 kJ/mol. The calculation, however, neglected the entropy term, and higher enthalpy values ~ 130 kJ/mol were estimated when the entropy term was taken into account.

Lee and Lee applied hydrogen TDA to Fe–Ti–C alloys in which the amounts of Ti and C varied in a wide range while fixing the Ti/C mass ratio at 4:1 [75]. Hydrogen charging was at 673 K under 0.1 MPa hydrogen gas, and successive aging at room temperature released the diffusive part of hydrogen. TDA of remaining hydrogen showed three desorption peaks at 473, 773, and 996 K at a heating rate of 3 K/min, and the 996 K peak was assigned to de-trapping from the incoherent TiC/matrix. The activation energy of de-trapping obtained from Kissinger's equation, Eq. (2.15), was 86.9 kJ/mol. The binding energy of hydrogen with TiC was calculated using the relation between the TDA peak area and the hydrogen-charging temperature T_H of the form,

$$C_x = N_x C_0 \exp\left(\frac{E_b - E_0}{RT_H}\right), \quad (3.19)$$

where C_x and C_0 are respectively concentrations of hydrogen trapped at TiC and in solid solution, N_x is the trap density, and E_0 is the heat of solution [75]. The estimated binding energy E_b^{TiC} and N_x are 28.1 kJ/mol and $10^{23}/\text{cm}^3\text{-Fe}$, respectively.

Successively, TDA was applied to specimens with controlled TiC/matrix interfaces [76]. Hydrogen introduced to a ferritic Fe–Ti–C alloy heat-treated at different austenitizing temperatures showed four desorption peaks at 383, 473, 748, and 880 K at a heating rate of 3 K/min. Two peaks at 748 K and 800 K were assigned to de-trapping from semicoherent and incoherent interfaces, respectively. It implies that the trapping strength of TiC increases associated with the loss of the particle/interface coherency. The hydrogen trapping energy at the incoherent interface is not always unique. The peak temperature assigned to the incoherent interface shifted to higher temperatures when specimens were further heat-treated to increase the TiC particle size.

In ferritic Fe–Ti–C alloys, incoherent TiC particles and Ti atoms in solution act as irreversible and reversible traps, respectively. The apparent hydrogen diffusion coefficient, obtained by the permeation transient, is often used to estimate the hydrogen

binding energy with traps as described in Sect. 3.1.1.2 concerning hydrogen permeation. A method devised to separate trapping parameters of reversible and irreversible traps was a sequential permeation method [77]. Both types of trapping take place in the first permeation, but reversible trapping dominates diffusivity in the second transient after irreversible traps have been filled. The difference between the first and the second transients gives irreversible trapping parameters. The obtained binding energies were 94.6 kJ/mol for incoherent TiC and 26 kJ/mol for reversible trap assigned to solute Ti atom [77].

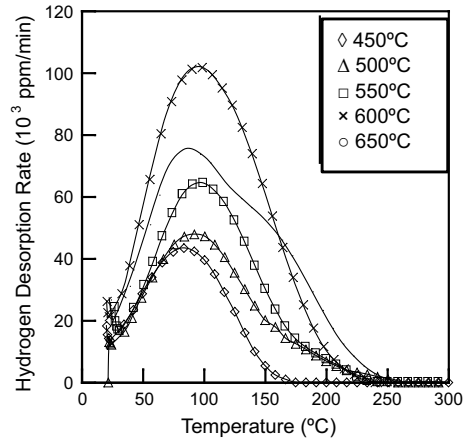
Precipitation of TiC on tempering of martensitic steel brings about a substantial increase in hydrogen absorption capacity. Hydrogen trapping of a TiC particle associated with its coherent-to-incoherent interfacial character transition was extensively studied for low-carbon steel [78]. Using TDA and transmission electron microscopy (TEM) together, Wei and Tsuzaki revealed that the broad semicoherent interface of the disk-like TiC traps 1.3 atoms/nm² hydrogen during cathodic charging for 1 h. The activation energy for hydrogen desorption from this semicoherent interface was 55.8 kJ/mol, the misfit dislocation core likely being the trap site. On the other hand, the hydrogen binding energy of incoherent TiC particles increased from 68 to 137 kJ/mol as the tempering temperature was raised from 737 to 973 K. A further increase in the tempering temperature to 1073 K decreased the binding energy to 85 kJ/mol. The amount of trapped hydrogen decreases with the increasing tempering temperature above 823 K, and TiC particles likely trap in themselves.

3.3.2 NbC and VC

NbC and VC of NaCl-type structures are also common precipitates in high-strength low-alloy steel, and their precipitation increases the hydrogen absorption capacities of steel. Desorption peak temperatures on TDA relevant to NbC and VC are generally lower than the peak temperature due to TiC [79, 80] but are often in the same range as the desorption from other traps. Determining the specific trapping parameters is then difficult, but lower peak temperatures imply lower binding energies of hydrogen with NbC and VC than that with TiC. Figure 3.17 [81] shows TDA profiles of hydrogen introduced to 0.37C–1.0Mo–0.54 V martensitic steel tempered at different temperatures. The precipitation of fine VC particles causes a prominent secondary hardening of martensite. Separately conducted hardness measurements and transmission electron microscopy revealed increased hydrogen absorption capacity associated with secondary hardening [80]. A distinct shoulder in the high-temperature side of the desorption peak for the 923 K (650 °C) tempering is ascribed to trapping at fine VC precipitates.

The Atom-Probe tomography to visualize hydrogen trapping at TiC and VC in precipitation-hardened steel is described in Sect. 2.3.2.3 [82, 83]. Hardening proceeded with time on isothermal aging at 883 K, showing a maximum at the aging time of 8 h. The trapping sites in the peak-aged steel with large trapping energy are around the (001) broad interface between VC precipitate and ferrite matrix. However,

Fig. 3.17 TDA profiles of hydrogen introduced to 0.37C-1.0Mo-0.54 V martensitic steel tempered at temperatures shown in the insert (Nagumo et al. [81])



no hydrogen trapping was observed in the under-aged steel with the small trapping energy. In simultaneously conducted TDA measurements, the evolution of a large desorption peak corresponded to peak aging.

Fine VC precipitates trap hydrogen at their interface with the ferrite matrix and in the surrounding stress fields, induced by both coherency of the interface and stress intensification by the precipitates. Figure 3.18 shows TDA profiles of hydrogen introduced to the same steel as used in Fig. 3.17, tempered at 550 °C (823 K) and 650 °C (923 K) [81]. The specimens were applied stress of 0.4 of the ultimate tensile strength before introducing the tracer hydrogen and aged at room temperature before TDA. In Fig. 3.18, the filled marks indicate TDA profiles after degassing at room temperature for 24 h. The difference between the open and filled marks is the amount of diffusive hydrogen.

TDA curves exhibit a single peak, but the peak widths are substantially wide. Room temperature degassing showed that hydrogen composing the higher temperature side of the peak is non-diffusive. A separately conducted measurement showed that the applied stress increased densities of both diffusive and non-diffusive hydrogen trap sites, the increase being more prominent for non-diffusive hydrogen [81].

In the case of fine precipitates, the number of hydrogen trap sites is high, and their distribution is uniform, increasing the average hydrogen absorption capacity of the steel. It must be careful that overall or average information from a specimen does not always represent local situations. Strongly trapped non-diffusive hydrogen is irrelevant to embrittlement, and hydrogen behaviors concerning hydrogen embrittlement in martensitic steel are described in Sect. 8.1.2.

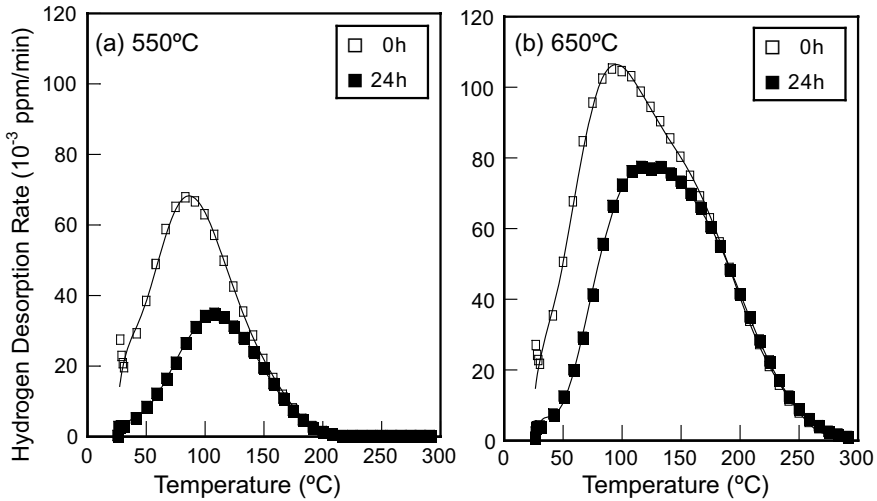


Fig. 3.18 TDA profiles of hydrogen introduced to 0.37C-1.0Mo-0.54 V martensitic steel tempered at (a) 550 °C (823 K) and (b) 650 °C (923 K). Hydrogen charging is conducted under applied stress of 0.4 tensile strength. Filled marks denote specimens kept for 24 h at 30 °C (303 K) to remove diffusive hydrogen (Nagumo et al. [81])

3.3.3 Fe_3C

Precipitation of fine Fe_3C hardly affects the hydrogen absorption capacity on the tempering of 0.42% C martensitic steel [78]. TDA profiles of hydrogen in eutectoid steel do not show trapping of hydrogen to pearlitic Fe_3C when cold-working is not applied, as shown in Fig. 2.8. It suggests that Fe_3C and its interface are not strong trap sites. On the other hand, two TDA peaks appeared by cold-drawing originating in fine lamellar Fe_3C . The cause of the evolution of the higher-temperature peak, increasing by cold-drawing, is the strain-induced formation of irreversible traps in the interface or within Fe_3C . A noteworthy fact is that such irreversibly trapped hydrogen or trapping defects are almost immune to hydrogen embrittlement.

3.4 Grain Boundaries

3.4.1 Experimental Works

Accumulation of hydrogen along grain boundaries has been revealed directly using autoradiography, shown in Fig. 2.16 for low-carbon ferritic steel. However, the type and structure of grain boundaries are diverse, and reported values of hydrogen binding energies with grain boundaries substantially scatter. Thermal desorption kinetics and

tritium autoradiography for ferritic Fe–Ti–C alloys showed that the release of tritium from grain boundaries took place below 573 K, and the calculated trapping energy was 59 kJ/mol neglecting the entropy term in the free energy change [74].

The hydrogen binding energy with ferrite grain boundaries was formerly reported by Choo and Lee using TDA for cold-worked and recrystallized iron with grain size controlled from two to nine in the ASTM numbers [15]. Hydrogen introduced at 673 K was partially degassed by room temperature aging. A TDA peak that appeared around 373 K, preceding the evolution of a large desorption peak, was assigned to grain boundaries. The activation energy of desorption obtained using Kissinger's equation was 17.2 kJ/mol, giving 9.6 kJ/mol for the binding energy after subtracting the saddle point energy of 7.6 kJ/mol. However, Kissinger's equation addresses the dissociation-controlled desorption of hydrogen, and the value of 9.6 kJ/mol is too small to apply the dissociation-controlled analysis. The experiment used the specimen of 8 mm in diameter and degassing at room temperature for six hours, likely diffusive hydrogen remaining in solution.

Alternatively, modeling of TDA profiles of hydrogen from pure iron with different grain sizes was conducted, assuming diffusion-controlled desorption [16], described in Sect. 2.2.1.3. The desorption-rate peak at 415 K was assigned to grain boundaries, and the binding energy of 49 kJ/mol gave the best fit between simulated and experimental TDA profiles.

3.4.2 Theoretical Works

Matsumoto et al. calculated the cohesive energy of symmetrical tilt grain boundaries in α -Fe under a gaseous hydrogen environment using density functional theory (DFT) [84]. The definition of the binding energy of hydrogen at a site x was the difference in the heat of solution between the position x and far from grain boundaries. Large gaps in high-energy grain boundaries capture many hydrogen atoms in these spaces. Calculated binding energies were 47.3, 32.8, and 45.3 kJ/mol for $\Sigma 3(111)$, $\Sigma 3(112)$, and $\Sigma 9(114)$ symmetrical tilt grain boundaries, respectively. However, the binding energy between hydrogen and grain boundaries is negligible when carbon and nitrogen atoms segregate at grain boundaries at their solubility limit, i.e., carbon and nitrogen atoms exclude hydrogen atoms from the grain boundaries.

The local coordination and the volume of the available interstitial sites influence hydrogen solubility within grain boundary regions. Du et al. examined the interaction of hydrogen with close-packed and open grain boundary structures in α - and γ -Fe, using DFT [85]. The structures or types of grain boundaries strongly affect the heat of solution of hydrogen within grain boundaries. Within the open grain boundary structures, like $\Sigma 5$ bcc and $\Sigma 11$ fcc, different interstitial sites are available, generally providing favorable binding sites for hydrogen atoms. Hydrogen accumulation at the grain boundary is energetically favored for those structures, implying hydrogen trapping in the grain boundary. The calculated hydrogen trap energies are ~ 40 and ~ 10 kJ/mol for $\Sigma 5$ bcc and $\Sigma 11$ fcc grain boundaries, respectively.

Grain-boundary-related results must be carefully examined in respect of situations surrounding boundaries, as described in Sect. 3.2.3.2(b) concerning observations of positron annihilation spectroscopy for Ni-alloys [67]. The presence of plastic strain is an item to be remarked on, and impurity segregation and precipitates often decorate grain boundaries. The role of grain boundaries in hydrogen embrittlement is to be considered, taking into account various associated factors, such as the cohesive strength of boundaries, their modifications by segregated impurities or precipitates, and concentrated plastic deformation in adjacent areas.

3.5 Voids and Surfaces

The precipitation of molecular hydrogen under high hydrogen fugacity activates small voids or cracks occasionally formed in metallic materials. De-trapping of deuterium from helium bubbles formed by ion implantation of 15-keV ^4He into iron and austenitic stainless steels was investigated by measuring the release of deuterium [50, 51]. The size of the bubbles was about 1 nm in diameter, and the thermal release of deuterium from the implanted zone was analyzed in the same way as described in Sect. 3.2.3.1. For iron, three types of traps were assumed, and the strongest trap with the binding enthalpy of 75 kJ/mol was assigned to de-trapping from He bubbles [50]. Similarly, in Type 304 stainless steel, the corresponding value was 41 kJ/mol assuming two types of traps [51].

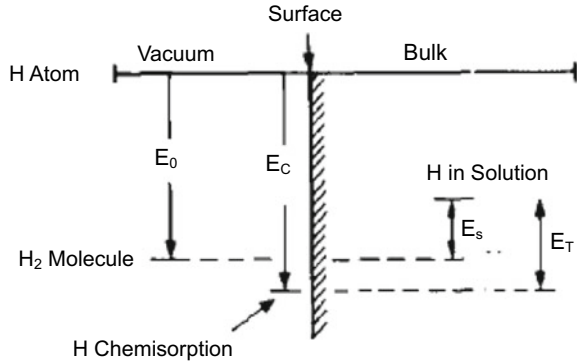
The precipitation of molecular hydrogen activates small voids. Adsorption on the void surface is an intermediate step in diffusing out of molecular hydrogen in voids, and the deuterium binding with the He bubble is considered a chemisorption-like interaction. The hydrogen binding energy with the bubble surface, E_T , is the lowered hydrogen energy relative to the lattice site, as illustrated in Fig. 3.19 [86]. It is written as

$$E_T = E_{\text{chem}} + E_s - \frac{1}{2}E_{\text{H}_2}, \quad (3.20)$$

where E_{chem} is the chemisorption binding energy of hydrogen referred to as the free hydrogen atom in a vacuum, E_s is the heat of solution, and E_{H_2} is the energy of hydrogen molecule. Using experimental values of $E_{\text{chem}} = 259$ kJ/mol and $E_s = 28$ kJ/mol together with $E_0 = 222$ kJ/mol for α -Fe, a calculated E_T is 77 kJ/mol [72]. The calculated value of E_T is consistent with the value obtained from the deuterium implantation experiment [50].

Visualization of hydrogen desorption from 5%Ni–Fe alloy by Krieger et al. using SKPFM [44] is described in Sect. 2.4.2. SKPFM for hydrogen introduced into specimens revealed hydrogen trapping at the interface of oxide inclusions in the cold-worked specimen. In a simultaneously conducted TDA measurement, Krieger et al. assigned the desorption peak of 38.5 ± 5 kJ/mol in the desorption binding energy to vacancies presumably generated along the interface of inclusions.

Fig. 3.19 Schematic illustration of hydrogen energies. E_T is the lowering of hydrogen energy by moving from solid solution to surface site (Picraux [86])



References

1. R. Gibara, A.J. Kumnick, in *Hydrogen Embrittlement and Stress Corrosion Cracking*, ed. by R. Gibara, R.F. Hehemann (ASM, Metals Park OH., 1984), pp. 61–77
2. T.S. Kê, *Scr. Metall.* **16**, 225–231 (1982)
3. V. Hivert, P. Groh, W. Frank, I. Ritchie, P. Moser, *Phys. Stat. Sol. (a)* **46**, 89–98 (1978)
4. G.M. Sturges, A.P. Miodownik, *Acta Metall.* **17**, 1197–1207 (1969)
5. J.P. Hirth, *Metall. Trans. A* **11A**, 861–890 (1980)
6. G. Schoek, *Scr. Metall.* **16**, 233–239 (1982)
7. A. Seeger, *Scr. Metall.* **16**, 241–247 (1982)
8. J.P. Hirth, *Scr. Metall.* **16**, 221–223 (1982)
9. A. Zielinski, E. Lunarska, M. Smialowski, *Acta Metall.* **25**, 551–556 (1977)
10. R. Gibara, *Trans. Metall. Soc. AIME* **239**, 1574–1585 (1967)
11. S. Asano, M. Shibata, *Scr. Metall.* **16**, 1171–1174 (1982)
12. L. Vandewalle, M.J. Konstantinović, T. Depover, K. Verbeken, *Steel Research Int.* **92** (2021). <https://doi.org/10.1002/srin.202100037>
13. R.A. Oriani, *Acta Metall.* **18**, 147–157 (1970)
14. A.J. Kumnick, H.H. Johnson, *Acta Metall.* **28**, 33–39 (1980)
15. W.Y. Choo, J.Y. Lee, *Metall. Trans. A* **13A**, 135–140 (1982)
16. K. Ono, M. Meshii, *Acta Metall.* **40**, 1357–1364 (1992)
17. Y. Sugiyama, K. Takai, *Acta Mater.* **208**, 116663 (2021)
18. J.P. Hirth, in *Hydrogen Degradation of Ferrous Alloys*, ed. by R.A. Oriani, J.P. Hirth, M. Smialowski (Noyes Pub., Park Ridge N.J. 1985), pp. 131–139
19. J.P. Hirth, B. Carnahan, *Acta Metall.* **26**, 1795–1803 (1978)
20. S. Taketomi, R. Matsumoto, N. Miyazaki, *Acta Mater.* **56**, 3761–3769 (2008)
21. J.W. Christian, *Metall. Trans. A* **14A**, 1237–1256 (1983)
22. M.S. Duesbery, V. Vitek, *Acta Mater.* **46**, 1481–1492 (1998)
23. M. Wen, A.H.W. Ngan, *Acta Mater.* **48**, 4255–4265 (2000)
24. S.L. Frederiksen, K.W. Jacobsen, *Phil. Mag.* **83**, 365–375 (2003)
25. M. Itakura, H. Kaburaki, M. Yamaguchi, *Acta Mater.* **60**, 3698–3710 (2012)
26. M. Wen, S. Fukuyama, K. Yokogawa, *Acta Mater.* **51**, 1767–1773 (2003)
27. M. Itakura, H. Kaburaki, M. Yamaguchi, T. Okita, *Acta Mater.* **61**, 6857–6867 (2013)
28. V.G. Gavriljuk, V.N. Shivanyuk, B.D. Shanina, *Acta Mater.* **53**, 5017–5034 (2005)
29. V.G. Gavriljuk, B.D. Shanina, V.N. Shivanyuk, S.M. Teus, *J. Appl. Phys.* **108**, 083723 (2010)
30. R. Kirchheim, *Acta Mater.* **55**, 5129–5138 (2007)
31. R. Kirchheim, *Acta Mater.* **55**, 5139–5148 (2007)
32. R. Kirchheim, *Scr. Mater.* **62**, 67–70 (2010)

33. H.J. Wollenberger, in *Physical Metallurgy 4th Ed. vol. II*, ed. by R.W. Cahn, P. Hansen, Chapter 18 (North-Holland, Amsterdam, 1996)
34. R.W. Siegel, J. Nucl. Mater. **69&79**, 117–146 (1978)
35. P. Hautojää, in *Characterization of Defects in Materials*, ed. by R.W. Siegel, J.R. Weertman, R. Sinclair, Materials Research Society Proceedings vol. 82 (MRS, 1987), pp. 3–21
36. A. Vehanen, P. Hautojärvi, J. Johansson, J. Yl-Kaupila, P. Moster, Phys. Rev. B **25**, 762–780 (1982)
37. L. De Schepper, D. Segers, L. Dorikens-Vanpraet, M. Dorikens, G. Knuyt, L.M. Stals, P. Moser, Phys. Rev. B **27**, 5257–5269 (1983)
38. J. Takamura, I. Takahashi, M. Amano, Trans. ISIJ **9**, 216–221 (1969)
39. H.G. van Bueren, Acta Metall **3**, 519–524 (1955)
40. A.M. Cuttiño, M. Ortiz, Acta Mater. **44**, 427–436 (1996)
41. U. Essmann, H. Mughrabi, Phil. Mag. A **40**, 731–756 (1979)
42. Y. Ohashi, Phil. Mag. **98**, 2275–2295 (2018)
43. M. Nagumo, K. Ohta, H. Saitoh, Scr. Mater. **40**, 313–319 (1999)
44. W. Krieger, S.V. Merzlikin, A. Bashir, A. Szczepaniak, H. Springer, M. Rohwerder, Acta Mater. **144**, 235–245 (2018)
45. J.R. Beeler Jr., R.A. Johnson, Phys. Rev. **156**, 677–684 (1967)
46. M.J. Puska, R.M. Nieminen, J. Phys. F: Met. Phys. **13**, 333–346 (1983)
47. M. Kiritani, H. Takata, K. Moriyama, F.E. Fujita, Phil. Mag. A **40**, 779–802 (1979)
48. R.W. Balluffi, J. Nucl. Mater. **69&70**, 240–263 (1978) (Overview)
49. S.M. Myers, S.T. Picraux, R.E. Stoltz, J. Appl. Phys. **50**, 5710–5719 (1979)
50. S.M. Myers, D.M. Follstaedt, F. Besenbacher, J. Böttiger, J. Appl. Phys. **53**, 8734–8744 (1982)
51. S.M. Myers, W.R. Wampler, F. Besenbacher, J. Appl. Phys. **56**, 1561–1571 (1984)
52. F. Besenbacher, J. Böttiger, S.M. Myers, J. Appl. Phys. **53**, 3536–3546 (1982)
53. F. Besenbacher, B.B. Nielson, S.M. Myers, J. Appl. Phys. **56**, 3384–3393 (1984)
54. S.M. Myers, F. Besenbacher, J. Appl. Phys. **60**, 3499–3507 (1986)
55. F. Besenbacher, J. Böttiger, B.B. Nielson, A.A. Pisarew, Phys. Rev. Lett. **49**, 1420–1422 (1982)
56. F. Besenbacher, S.M. Myers, P. Nordlander, J.K. Nørskov, J. Appl. Phys. **61**, 1788–1794 (1987)
57. P. Nordlander, J.K. Nørskov, F. Besenbacher, S.M. Myers, Phys. Rev. B **40**, 1990–1992 (1989)
58. Y. Tateyama, T. Ohno, Phys. Rev. B **67**, 174105 (2003)
59. R. Matsumoto, N. Nishiguchi, S. Taketomi, N. Miyazaki, J. Soc. Mater. Sci. Jpn. **63**, 182–187 (2014)
60. E. Hayward, B. Beeler, C. Deo, Phil. Mag. Lett. **82**, 217–225 (2012)
61. K. Ebihara, Y. Sugiyama, R. Matsumoto, K. Takai, T. Suzudo, Metall. Mater. Trans. A **52A**, 257–269 (2021)
62. K. Takai, H. Shoda, H. Suzuki, M. Nagumo, Acta Mater. **56**, 5158–5167 (2008)
63. Y. Sato, T. Doshida, H. Suzuki, K. Takai, Y. Hagihara, CAMP ISIJ **23**, 1292 (2010)
64. K. Sakaki, T. Kawase, M. Hirano, M. Mizuno, H. Araki, Y. Shirai, M. Nagumo, Scr. Mater. **55**, 1031–1034 (2006)
65. C. Hidalgo, G. González-Doncel, S. Linderroth, S. San Juan, Phys. Rev. B **45**, 7017–7021 (1992)
66. K. Sugita, M.Y. Shirai, J. Physics, Conf. Ser. **674**, 012006 (2016)
67. S.K. Lawrence, Y. Yagodzinskyy, H. Hänninen, E. Korhonen, F. Tuomisto, Z.D. Harris, B.P. Somerday, Acta Mater. **128**, 218–226 (2017)
68. L. Chiari, A. Nozaki, K. Koizumi, M. Fujinami, Mater. Sci. Eng., A **800**, 140281 (2021)
69. M. Hatano, M. Fujinami, K. Arai, H. Fujii, M. Nagumo, Acta Mater. **67**, 342–353 (2014)
70. A. Komatsu, M. Fujinami, M. Hatano, K. Matsumoto, M. Sugeoi, L. Chiari, Int. J. Hydrogen Energy **46**, 6960–6969 (2021)
71. L. Chiari, A. Komatsu, M. Fujinami, ISIJ Int. **61**, 1927–1934 (2020)
72. K. Saito, T. Hirade, K. Takai, Metall. Mater. Trans. A **50A**, 5091–5102 (2019)
73. C.R. Luna, C. Macchi, A. Juan, A. Somoza, J. Phys. Conf. Ser. **443**, 012019 (2013)
74. T. Asaoka, C. Dagbert, M. Autocoururier, J. Galland, Scr. Metall. **11**, 467–472 (1977)
75. H.G. Lee, J.Y. Lee, Acta Metall. **32**, 131–136 (1984)
76. S.M. Lee, J.Y. Lee, Acta Metall. **35**, 2695–2700 (1987)

77. G.M. Pressouyre, I.M. Bernstein, *Metall. Trans. A* **9A**, 1571–1580 (1978)
78. F.-G. Wei, K. Tsuzaki, *Metall. Mater. Trans. A* **37**, 331–353 (2006)
79. T. Omura, T. Kushida, K. Miyata, Y. Komizo, *Tetsu-to-Hagané* **90**, 106–112 (2004)
80. T. Tsuchida, T. Hara, K. Tsuzaki, *Tetsu-to-Hagané* **88**, 771–778 (2002)
81. M. Nagumo, T. Tamaoki, T. Sugawara, in *Hydrogen Effects on Materials Behavior and Corrosion Deformation Interactions*, ed. by N.R. Moody, A.W. Thompson, R.E. Ricker, G.W. Was, R.E. Jones (TMS, Warrendale OH, 2003), pp. 999–1008
82. J. Takahashi, K. Kawakami, Y. Kobayashi, T. Tarui, *Scripta Mater.* **63**, 261–264 (2010)
83. J. Takahashi, K. Kawakami, Y. Kobayashi, *Acta Mater.* **153**, 193–204 (2018)
84. R. Matsumoto, M. Riku, S. Taketomi, N. Miyazaki, *Prog. Nucl. Sci. Tech.* **2**, 9–15 (2011)
85. Y.A. Du, L. Ismer, J. Rogal, T. Hickel, J. Neugebauer, R. Drautz, *Phys. Rev. B* **84**, 144121 (2011)
86. S.T. Picraux, *Nucl. Instru. Methods* **182/183**, 413–437 (1981)